



Effect of NaF and CaO/SiO₂ Mass pct. on the Hydrogen Dissolution Behavior in Calcium-Silicate-Based Molten Fluxes

Sung Hoon Chung¹ · Il Sohn¹

Received: 3 February 2019 / Accepted: 8 May 2019 / Published online: 16 May 2019
© The Korean Institute of Metals and Materials 2019

Abstract

The effect of NaF and CaO/SiO₂ mass pct. ratio (C/S) on the hydrogen solubility in terms of the hydroxyl capacity of the CaO–SiO₂–NaF welding flux system was investigated at 1823 K. As a cost-effective alternative to CaF₂ in welding fluxes, NaF can potentially increase the fluidity, electrical conductivity, and hydroxyl capacity of welding fluxes in advanced high-strength steels. Additions of 1.9 to 5.9 mass pct. of NaF was found to depolymerize the structural units in the flux system. Depending on the flux composition, the dominant hydrogen dissolution mechanism varied. At C/S values less than 1.06, the incorporated-hydroxyl dissolution mechanism was dominant in the present flux system, in which SiO₂-based complex structural units were pronounced. At C/S values above 1.06, the free-hydroxyl dissolution mechanism was pronounced due to the strong network-modifying CaO content supplemented by NaF. A combination of Fourier transformed infrared, Raman, X-ray photoelectron spectroscopy and time of flight secondary ion mass spectrometry analysis was used to determine the structural implications of NaF additions and C/S, which were correlated to the hydroxyl capacity of the flux. High NaF contents and C/S values were found to depolymerize the complex structural units of the molten flux by supplying greater amounts of network-modifying free oxygen (O²⁻) and fluorine (F⁻) anions to the flux system in the compositional range of this work.

Keywords Hydroxyl capacity · Welding flux · NaF · Incorporated-hydroxyl · Free-hydroxyl · Structural units

1 Introduction

Next-generation advanced high-strength steel (AHSS) utilizing deformation twinning contains significant amounts of Mn and Al to improve formability and attain high strength above 1 GPa [1–3]. However, the high strength and formability required for these AHSS materials have also been associated with a high sensitivity to hydrogen embrittlement [4–6] and induced cracking along the grain boundaries and interfaces between the weld zone [7]. Thus, hydrogen control for these relatively new steel grades is a critical issue to be resolved before widespread commercialization can occur.

During the welding process, sources of hydrogen have been identified to be the filler metal, atmospheric moisture, welding fluxes and the lubricant used in the manufacture of fluxed welding rods [8]. Filler metals typically contain less than 2 ppm hydrogen, and with proper pre-drying,

physisorbed moisture in welding fluxes is removed. Thus, the main source of hydrogen is atmospheric moisture and the lubricant used, which may be prevalent under certain welding conditions.

So et al. [9] described the use of high-Mn-containing steels to absorb significant amounts of hydrogen at temperatures below 373 K compared with the use of low-carbon steels. Therefore, minimizing the dissolved hydrogen within the weld metal and substrate is essential to ensuring the quality of the weld [10, 11]. Minimizing this hydrogen content can be accomplished by optimizing the welding flux such that it has a high capacity for hydrogen dissolution, which can maximize hydrogen removal from the weld zone. If the welding flux is not optimized for hydrogen removal, the hydrogen content in the weld zone [12–14] can exceed the critical condition for hydrogen embrittlement to occur.

Beyond welding, excessive dissolution of hydrogen in steels can disrupt the continuous casting process, in which molten steel is solidified into a semi-finished product [15]. The addition of alloying elements to modify the steel chemistry under humid conditions can add appreciable amounts of hydrogen to the steel [16], and during casting, excessive amounts of

✉ Il Sohn
ilsohn@yonsei.ac.kr

¹ Materials Science and Engineering, Yonsei University, Seoul 03722, Republic of Korea

hydrogen and nitrogen can form bubbles entrapped within the thin layer of the mold flux. These bubbles have lower conductivity and can also accelerate the crystallization of cuspidine ($\text{Ca}_4\text{Si}_2\text{O}_7\text{F}_2$), decreasing the heat flux, which can exacerbate caster breakouts [17].

Studies have shown hydrogen dissolution in molten fluxes to be strongly dependent on chemical composition [18] and the structure of the flux [19–24]. Hydrogen can dissolve in molten fluxes in the form of incorporated or free hydroxyl depending on the basicity (typically defined as the CaO/SiO_2 mass pct. ratio). In acidic fluxes or at low basicity, H_2O can react with the bridged oxygen (O^0) of the silicate network structure, forming an incorporated hydroxyl ($\text{Si}-\text{OH}$). Thus, greater hydrogen dissolution in an acidic flux can be realized with higher O^0 activity or lower basicity in the case of incorporated hydroxyl. In basic fluxes or at high basicity, H_2O can react with the free oxygen (O^{2-}) dispersed within the molten flux and produce free hydroxyls (OH^-). Accordingly, greater hydrogen dissolution in a basic flux can be realized with higher O^{2-} activity or higher basicity in the case of free hydroxyl [25, 26]. Past studies have focused on steelmaking slag systems, and structural analyses have been limited to FTIR and Raman [27–30] studies. Park et al. [31], identified the effect of CaF_2 fluidizers to a calcium-silicate melt, where hydrogen dissolution increased with higher CaF_2 content owing to the depolymerization of the melt structure and subsequent increase in the activity of O^{2-} . Furthermore, considering the importance of electrical conductivity for arc welding fluxes, halide fluidizers such as CaF_2 and NaF are known to stabilize the weld arc, while increasing the solubility of hydrogen in the fluxes. However, few studies have looked at hydrogen dissolution of NaF -containing calcium-silicate melts to the current authors' knowledge, which could be a cost-effective halide-containing welding flux system.

In this study, the hydrogen solubility in terms of the hydroxyl capacity (C_{OH}) of calcium-silicate fluxes containing NaF at 1823 K was studied under a flow of wet UHP Ar gas with a H_2O partial pressure of 0.2 atm. The effect of CaO/SiO_2 mass pct. ratio (C/S) between 0.65 to 1.5 and NaF contents between 1.4 to 5.9 mass pct. on the hydroxyl capacity and its correlation to the network structure were assessed. Structural analysis of the molten flux was evaluated by using a combination of various spectroscopic methods including FTIR (Fourier transformed infrared) spectroscopy, Raman spectroscopy, and XPS (X-ray photoelectron spectroscopy). In addition, a new approach to quantifying the OH^- and $\text{Si}-\text{OH}$ bonds by using TOF-SIMS (time of flight secondary ion mass spectrometry) was also conducted.

2 Experimental Methods and Procedures

2.1 Sample Preparation and Method

Flux samples were produced by using reagent-grade CaO , SiO_2 and NaF . 20 g of mixed samples were pre-melted at 1823 K in ultra-high-purity Ar (99.9999%) at 0.2 slm (standard litre per minute) in a Pt crucible for 5 h to ensure a homogeneous flux. The pre-melted flux was removed from the furnace and quenched in liquid nitrogen. The as-quenched flux was pulverized to a powder with a particle size smaller than 100 μm . Pre- and post-chemical composition was analyzed by X-ray fluorescence (XRF S4 Explorer; Bruker AXS GmbH, Karlsruhe, Germany), as shown in Table 1. NaF was the main component to change, when comparing the pre- and post-chemical composition. Thus, the results of the present work refer to the post-experimental compositions unless stated otherwise. A schematic of the experimental apparatus is shown in Fig. 1.

A Kanthal® vertical resistance furnace was used under 0.2 slm flow of ultra-high-purity Ar gas, which was passed through a sufficiently large humidifying vessel maintained at 333 K. The water-saturated Ar resulted in a H_2O partial pressure of 0.2 atm. [31–33]. The temperature was calibrated with a reference B-type thermocouple, and the target temperature was controlled using a PID (proportional integral derivative) controller within ± 3 °C. Preliminary equilibration experiments showed that the dissolution of hydrogen in the flux reaches thermo-chemical equilibrium after 5 h at 1823 K. After equilibration, the flux sample was quenched in liquid nitrogen to obtain an amorphous sample for structural analysis. The XRD of a typical as-quenched flux sample is also shown in Fig. 1, with broad characteristic XRD peaks that correspond to a fully amorphous state. Samples were kept inside an Ar-gas-purged vacuum box and the hydrogen content was analyzed within 48 h. The total hydrogen content in the flux was analyzed using a hydrogen analyzer (RH-600; LECO, MI, USA), which has been verified to provide accurate hydrogen analyses in fluxes [10, 31–33].

2.2 Structural Analysis Using FTIR and Raman Spectroscopy

FTIR (Spectra100; Perkin-Elmer, Shelton CT, USA) spectroscopy was used to qualitatively identify the structural units comprising the as-quenched flux at 1823 K (1550 °C). Under the conditions of the present study, the FTIR analysis focused on the range of 1400–400 cm^{-1} , which captures the frequencies at which Si–O stretching and bending vibrations occur. To supplement the FTIR analysis, semi-quantitative Raman (PD-RSM300; Photon Design, Tokyo,

Table 1 Pre- and post-experimental composition of the CaO–SiO₂–NaF ternary flux system using XRF equilibrated with Ar–0.2H₂O gas atmosphere

No.	Pre-experimental comp. (mass pct.)			Post-experimental comp. (mass pct.)			H (mass ppm)		CaO/SiO ₂ (pre/post)	C _{OH}	
	NaF	CaO	SiO ₂	NaF	CaO	SiO ₂	AVG	STDEV		AVG	STDEV
NCS1	3.0	36.4	60.6	1.9	38.5	59.5	67.9	3.0	0.6/0.65	1366.5	60.4
NCS2	3.0	43.1	53.9	1.9	45.3	52.8	63.1	1.6	0.8/0.86	1269.9	32.2
NCS3	3.0	48.5	48.5	1.7	50.7	47.6	61.1	1.2	1.0/1.06	1229.6	24.1
NCS4	3.0	52.9	44.1	1.5	55.3	43.3	63.3	0.7	1.2/1.28	1273.9	14.1
NCS5	3.0	56.6	40.4	1.4	58.7	39.9	62.7	1.5	1.4/1.47	1261.8	30.2
NCS6	6.0	35.3	58.7	4.1	37.5	58.4	62.7	1.0	0.6/0.64	1261.8	20.1
NCS7	6.0	41.8	52.2	3.9	44.4	51.7	60.5	1.2	0.8/0.86	1217.5	24.1
NCS8	6.0	47.0	47.0	4.2	49.5	46.3	59.8	1.1	1.0/1.07	1203.5	22.1
NCS9	6.0	51.3	42.7	3.4	54.2	42.4	64.7	1.1	1.2/1.28	1302.1	22.1
NCS10	6.0	54.8	39.2	3.4	57.9	38.7	64.4	1.2	1.4/1.5	1296.0	24.1
NCS11	9.0	34.1	56.9	5.9	37.0	57.1	61.8	0.9	0.6/0.65	1243.7	18.1
NCS12	9.0	40.5	50.6	5.5	43.6	50.9	62.0	1.2	0.8/0.86	1247.7	24.1
NCS13	9.0	45.5	45.5	5.0	49.2	45.8	63.3	0.8	1.0/1.07	1273.9	16.1
NCS14	9.0	49.6	41.4	4.3	53.7	42.0	65.6	1.0	1.2/1.28	1320.2	20.1
NCS15	9.0	53.1	37.9	4.2	57.3	38.5	67.7	1.8	1.4/1.49	1362.4	36.2

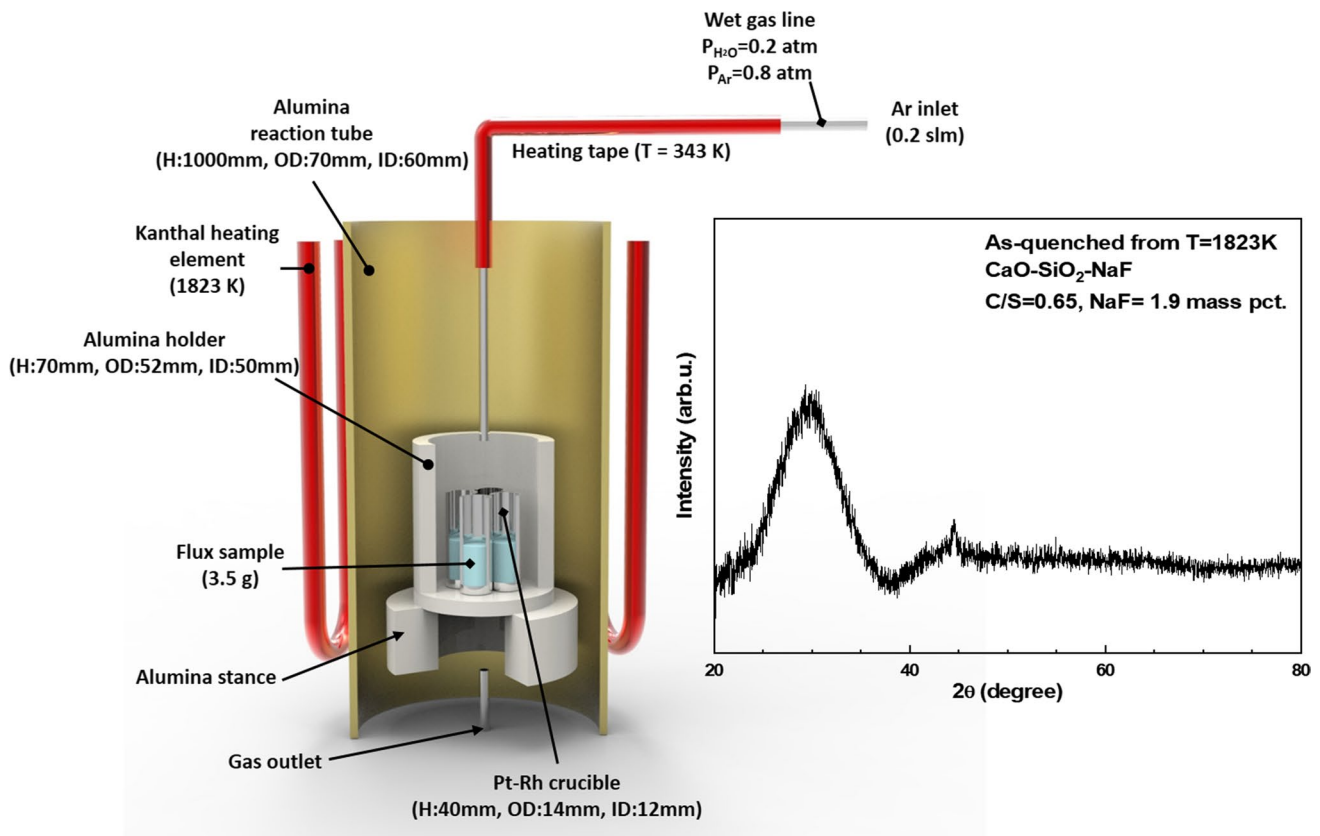


Fig. 1 Schematic of the experimental equipment and characteristic XRD peak of a typical as-quenched CaO–SiO₂–1.9NaF flux sample from 1823 K at C/S of 0.65

Japan) spectroscopy equipped with a 514 nm blue laser was also used. Details of the sample preparation for FTIR and Raman spectroscopy with the deconvolution procedure has been outlined in past works [10, 31–34].

2.3 Structural Analysis with XPS and TOF-SIMS

In addition to FTIR and Raman spectroscopy, XPS and TOF-SIMS were used for semi-quantitative analysis of the distribution of oxygen anion species and hydroxyls. Using XPS analysis, the fractions of free (O^{2-}), non-bridged (O^-), and bridged (O^0) oxygen anions were identified. The proportion of oxygen anions within the structural units can indirectly determine the dominant hydrogen dissolution mechanism that occurs in oxide melts. The binding energies corresponding to O^{2-} , O^- and O^0 were located over the ranges 529.79–530.29 eV, 531.33–531.75 eV and 532.51–532.84 eV, respectively. An $AlK\alpha$ source was used and the C_{1s} core binding energy at 285 eV was adopted for calibration.

TOF-SIMS (TOF-SIMS5; Ion tof GmbH, Münster, Germany) were obtained for as-quenched flux samples within a mass range of 0–700 m/e. Like XPS, TOF-SIMS is a surface-sensitive analytical method that excites and accelerates secondary ions and measures the mass by determining the time of flight required to reach the detector [35]. The advantage of TOF-SIMS is the ability to detect elements and molecules, and provide detailed chemical information on the surface of samples. When a primary ion hits a flux surface and penetrates into the surface region, a secondary ion is ejected with the fracture of the surface. A total ion dose of 60 keV Bi^{3+} primary ion beam was used with beam dimensions of $300\ \mu m \times 300\ \mu m$. The average total count for each specimen was 600,000. TOF-SIMS spectra of a

representative flux sample with various molecular masses of H^+ , OH^- , and $SiOH^-$ and various oxygen contents were also evaluated in the present work [34].

3 Results and Discussion

3.1 Effect of NaF on the Hydroxyl Capacity

Figure 2a, b shows the hydroxyl capacity ($C_{OH} = (\text{mass ppm } H_2O / (P_{H_2O})^{0.5})$ [24]) as a function of NaF content for C/S between 0.65 and 1.48 at 1823 K. At C/S below 0.86, the hydroxyl capacity decreased with higher NaF, as shown in Fig. 2a. At low C/S or high SiO_2 content, the acidic flux consists of complex network structural units with greater amounts of O^0 , where incorporated-hydroxyl sites are prevalent. Thus, additions of network-modifying NaF decreases the ability of the flux to dissolve hydrogen for the incorporated-hydroxyl dominant mechanism. At C/S above 1.06, the basic flux consists of simpler structural units with greater amounts of O^{2-} , where the free-hydroxyl is the dominant hydrogen dissolution mechanism. According to Chung et al. [34], the addition of NaF to a flux typically modifies the complex structural units and depolymerizes the network structure and releases O^{2-} into the melt. Thus, the addition of networking-modifying NaF will tend to increase the activity of O^{2-} and promote hydrogen dissolution in the free-hydroxyl dominant region, as shown in Fig. 2b. Similar trends can be observed in the $CaO-SiO_2-NaF-Al_2O_3$ system. For C/S between 0.86 and 1.06, as shown in Fig. 2a, both incorporated- and free-hydroxyl coexist in this transition region, and no single hydrogen dissolution mechanism is particularly dominant. Thus, depending on the content of NaF, the hydroxyl capacity can decrease or increase, and a

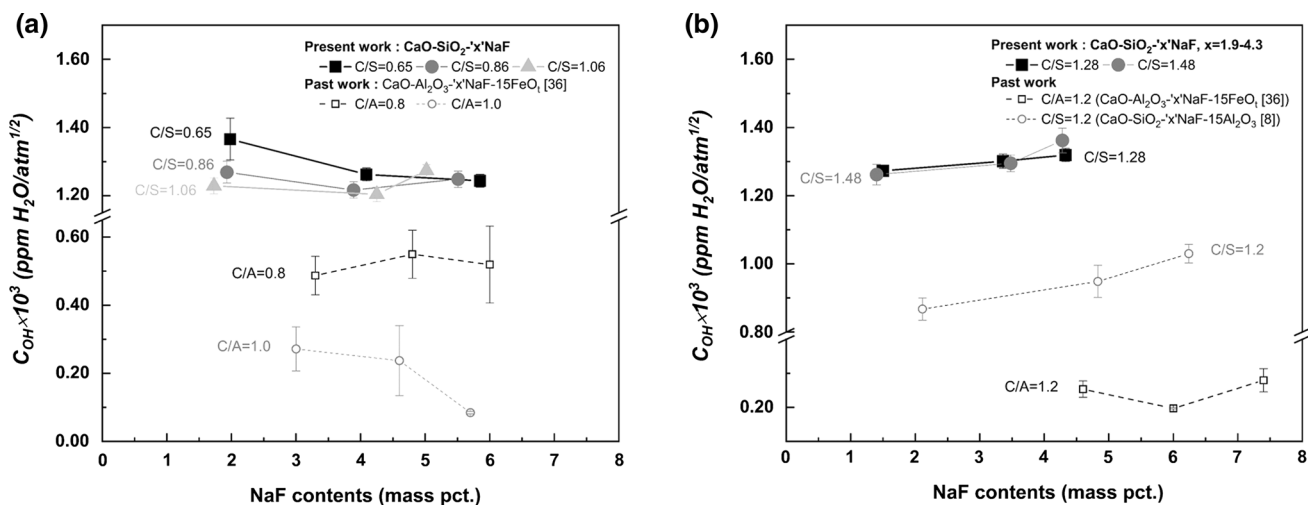


Fig. 2 Hydroxyl capacity in the $CaO-SiO_2-NaF$ system at 1823 K as a function of NaF at C/S between a 0.65 to 1.06 and b 1.28 to 1.48

transition can be observed, showing a minimum for these intermediate compositional ranges.

In comparison to the past work on $\text{CaO-Al}_2\text{O}_3-15\text{FeO}_1\text{-NaF}$ quaternary system [36], the effect of NaF in calcium-silicate based melts is much more pronounced and the hydroxyl capacity in calcium-aluminate melts as incorporated hydroxyls is not significant. This suggests that Al–OH bonding is thermodynamically unfavorable and that for calcium-aluminate based systems, which can be used in high-Al containing steel welding fluxes, additions of SiO_2 may be needed for NaF to have an appreciable effect on the hydroxyl capacity in the incorporated hydroxyl dominant regimes.

3.2 Effect of CaO/SiO₂ Mass pct. Ratio on Hydroxyl Capacity at Comparable NaF Contents

Figure 3a, b shows the hydroxyl capacity as a function of C/S at low and high NaF contents, respectively. With low additions of NaF between 1.4 and 4.2 mass pct., the variation of the hydroxyl capacity with C/S shows a parabolic concave upward trend with a minimum near C/S of unity. Due to the changes in the post-experimental NaF content compared with the weighed amount, NaF contents were divided into two groups with comparable NaF contents between 1.4 to 1.9 and between 3.4 to 4.2, which showed similar trends. At C/S between 0.65 and 0.86, the hydroxyl capacity decreased with higher C/S because in the acidic region of the flux, incorporated hydroxyl is the dominant hydrogen dissolution mechanism. As the C/S is increased, the activity of O^0 decreases, reducing the number of available incorporated hydroxyl sites in the flux. Beyond a C/S of 1.07, the dominant hydrogen dissolution mechanism was the free hydroxyl reaction, and higher C/S led to an increase in

the activity of O^{2-} , increasing the number of reaction sites for free hydroxyl and thus increasing the hydroxyl capacity in the flux. With NaF additions between 4.3 and 5.9, considered comparable NaF contents, sufficient fluorine anions were available to decouple the O^0 within the flux, further simplifying the network structure and limiting the available incorporated hydroxyl sites within the flux. Thus, at high NaF additions, the overall hydrogen dissolution mechanism of incorporated hydroxyl was negligible and shifted towards the free hydroxyl reaction and higher C/S led to an increase in the hydroxyl capacity. These results are similar to those reported by Chung et al. [34], Jo and Kim [37], and Schwedtfeger and Shubert [24] shown in Fig. 3a, b.

3.3 Effect of NaF on the Structural Units of the Melt

The flux composition can significantly change the hydrogen solubility in molten fluxes and can also greatly affect the structural units comprising the flux. Depending on the available O^0 and O^{2-} within the flux, the prominent hydrogen solubility mechanism can be determined. The results of FTIR analyses at various NaF contents and fixed C/S of 0.65 are shown in Fig. 4. Adding greater amounts of NaF at low C/S to the acidic fluxes increased the simpler silicate structures with an NBO/Si (non-bridged oxygen per silicon) ratio of 4 (Q^0), corresponding to the band between 850 and 880 cm^{-1} . The depth profile for NBO/Si = 1, 2, 4 and Si–O–Si bending is shaded in the figure and marked. The NBO/Si ratio of 3 was not relatively pronounced in this study. The ratio of NBO/Si = 1 to NBO/Si = 2 can be a qualitative indicator of the polymerization degree. According to Mysen et al.

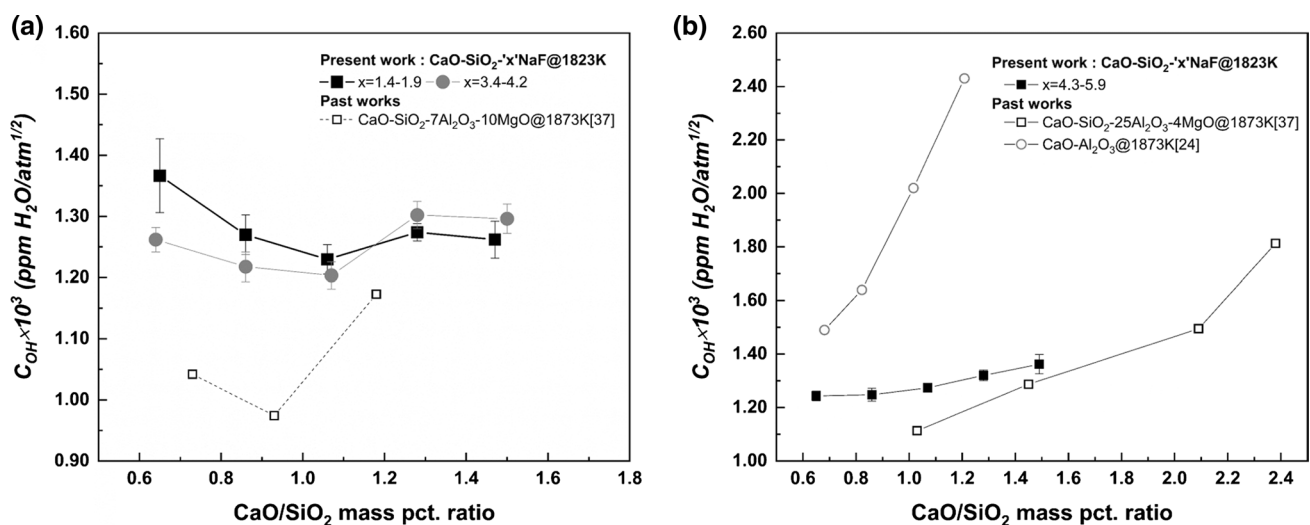


Fig. 3 Hydroxyl capacity at 1823 K in the $\text{CaO-SiO}_2\text{-NaF}$ system as a function of C/S at **a** low and **b** high NaF contents. Note similar trends observed in past works [24, 37] for different slag systems

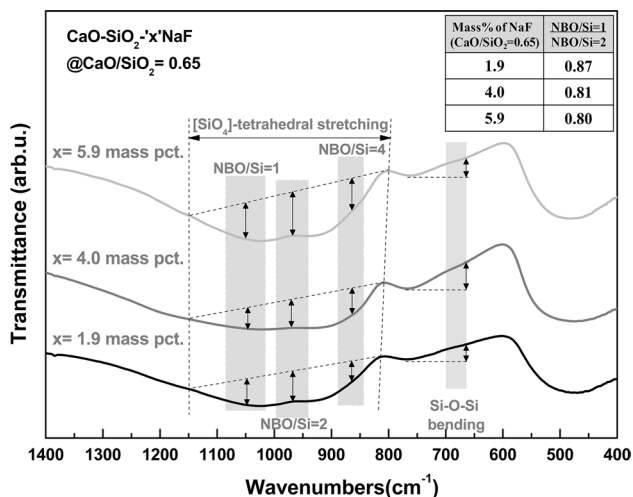
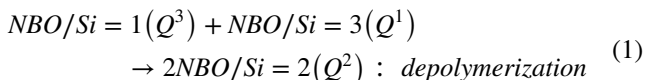


Fig. 4 FTIR results of as-quenched fluxes from 1823 K at various mass pct. of NaF in the CaO–SiO₂ based flux system at fixed C/S of 0.65

[38], the depolymerization of high-temperature melts can be expressed by the following reaction (1).



With an increase in the added NaF content from 1.9 to 5.9 mass pct., the ratio of NBO/Si = 1 to NBO/Si = 2 decreased from 0.87 to 0.8 [39]. To conduct a more semi-quantitative analysis of the structural units, Raman spectroscopy was conducted to complement the FTIR analysis.

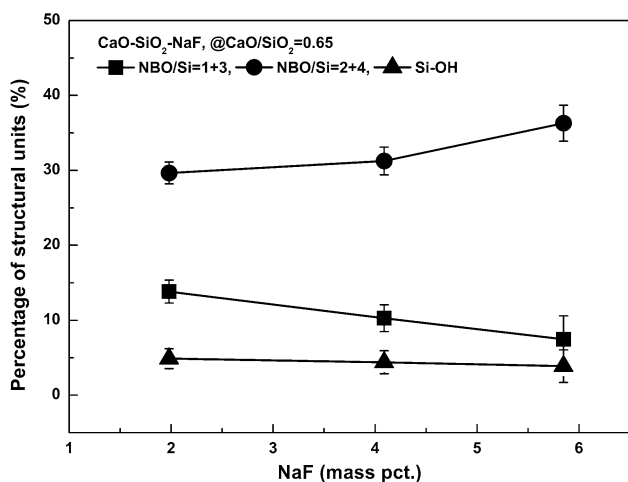
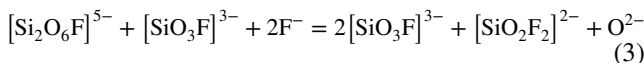
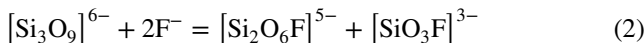


Fig. 5 Percentage of structural units after deconvolution of the Raman spectra for as-quenched CaO–SiO₂–NaF fluxes from 1823 K as a function of NaF at fixed C/S of 0.65

Figure 5 shows the percentage of structural units after deconvolution of the Raman spectra as a function of NaF content at fixed C/S of 0.65. The results indicate a decreasing trend of the NBO/Si = 1 + 3 (Q³ + Q¹) ratio and incorporated hydroxyl (Si–OH), which suggests that the number of complex structural units in the flux decreased. The opposite trend was observed for the comparatively simpler structure of NBO/Si = 2 (Q²) and NBO/Si = 4 (Q⁰). The Raman results correlate well with the results of the previous FTIR analysis.

Figure 6 shows the percentage of structural units after deconvolution of the XPS spectra as a function of NaF at fixed C/S of 0.65. A C/S of 0.65 was within the acidic region of the flux, where the incorporated hydroxyl mechanism was pronounced.

Analysis of the oxygen anion species indicated higher fractions of O²⁻ and O⁻ with increasing NaF. Ueda et al. [40] and Park and Min [41] suggested that the addition of fluorine compounds to a flux system can behave as a network modifier according to reactions (2) and (3).



Fluorine anions supplied by NaF can depolymerize the network structure of the flux and simplify the structural units. With excess O²⁻ formed according to reaction (3), a subsequent reaction with O⁰ can occur via reaction (4), as reported by Toop and Samis [42].

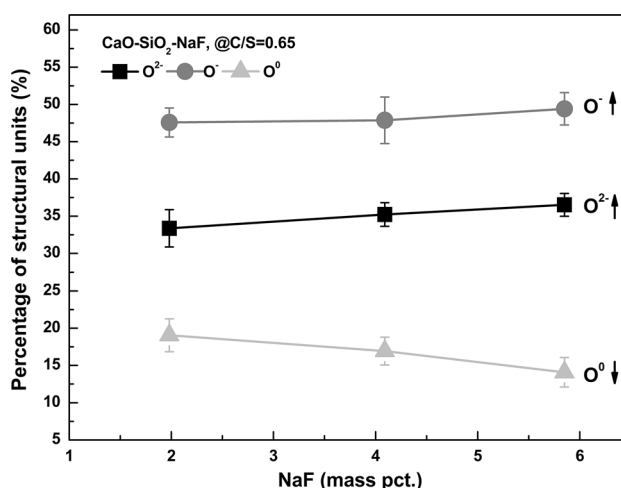
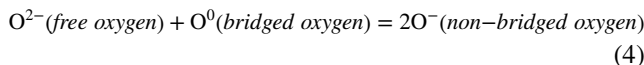


Fig. 6 Percentage of structural units after deconvolution of the XPS spectra for as-quenched CaO–SiO₂–NaF fluxes from 1823 K as a function of NaF at C/S of 0.65

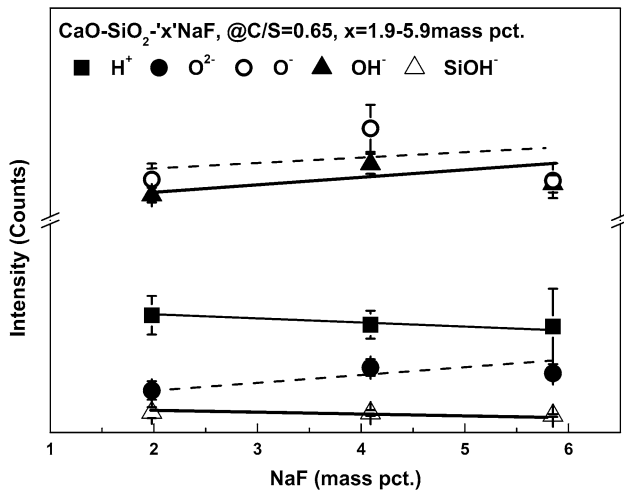


Fig. 7 TOF-SIMS spectra for as-quenched CaO–SiO₂–NaF fluxes from 1823 K as a function of NaF at fixed C/S of 0.65

In addition to XPS, TOF-SIMS can further complement the structural analysis by semi-quantitatively measuring the various anionic and cationic species existing on the surface of a sample.

Figure 7 shows the TOF-SIMS spectra as a function of the NaF content at fixed C/S of 0.65. TOF-SIMS is typically performed on polymer and thin-film surfaces to determine the surface chemical composition and the complexed structure of the surface. Slag and flux samples were analyzed by XPS and NMR, but in this case, Si–OH and OH– peaks were difficult to detect below a hydroxyl content of 30 ppm. However, TOF-SIMS can detect contents of 0.1 to 100 ppm of each hydroxyl and other small structures. Moreover, quantification can be performed with an optimized standard sample [35]. The results pertaining to positively and negatively charged species, including H⁺, various oxygen anions (O²⁻ and O⁻) and hydroxyls (OH⁻, SiOH⁻), could be obtained. H⁺ decreased with increasing NaF content. The number of incorporated hydroxyls (Si–OH) decreased as the amount of O²⁻ increased.

3.4 Effect of CaO/SiO₂ Mass pct. Ratio on the Structural Units of the Melt

FTIR results for the calcium-silicate flux system containing NaF contents between 1.4 and 1.9 at various C/S are shown in Fig. 8. The stretching vibrations of the [SiO₄]-tetrahedral structural units and Si–O–Si bending were clearly affected by an increase in the C/S. The stretching band for NBO/Si=4 near 850 cm⁻¹ increased with C/S. The ratio of NBO/Si=1 to NBO/Si=2 also decreased with an increase in the C/S. This lower (NBO/Si=1)/(NBO/Si=2) ratio suggests depolymerization of the network structure comprising the flux. A higher C/S provided greater amounts of network-modifying

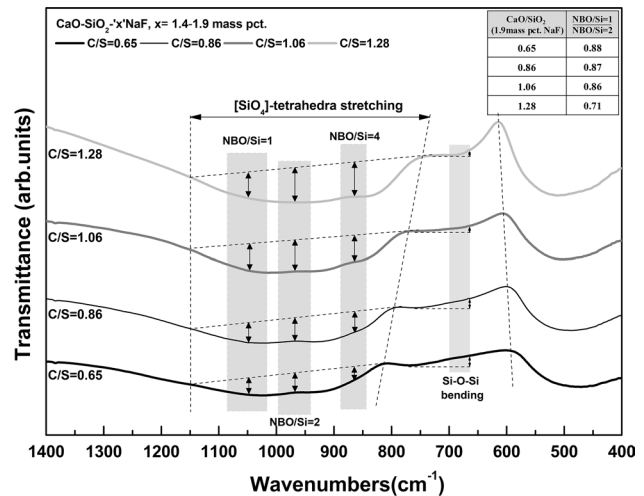


Fig. 8 FTIR results of CaO–SiO₂–1.4–1.9 mass pct. NaF fluxes at various C/S as-quenched from 1823 K

O²⁻ and the depth of the Si–O–Si bending band, located near 680 cm⁻¹, also decreased with an increase in the C/S, indicating that depolymerization occurred.

Figure 9 shows the percentage of structural units after deconvolution of the Raman spectra as a function of C/S in the CaO–SiO₂–1.4–1.9 mass pct. NaF flux system. The NBO/Si=1+3 and Si–OH stretching vibration, which correlate with the complexity of the network structure, decreased with an increase in the C/S. At higher C/S, network-modifying O²⁻ was supplied by CaO. Thus, greater amounts of available O²⁻ within the flux could interact with O⁰, diminishing the number of possible incorporated hydroxyl sites

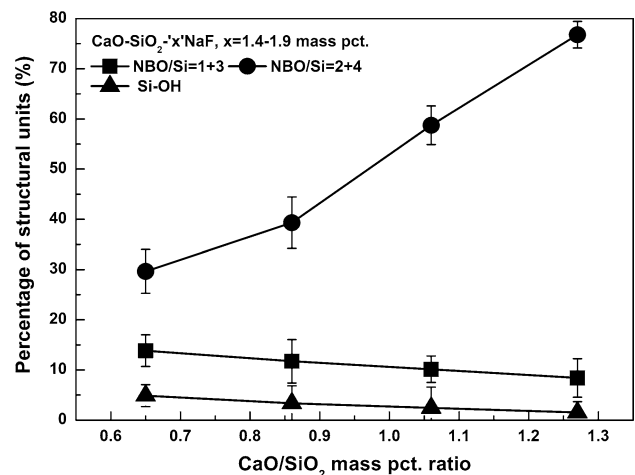


Fig. 9 Percentage of structural units after deconvolution of the Raman spectra for as-quenched CaO–SiO₂–1.4–1.9 mass pct. NaF fluxes from 1823 K as a function of C/S

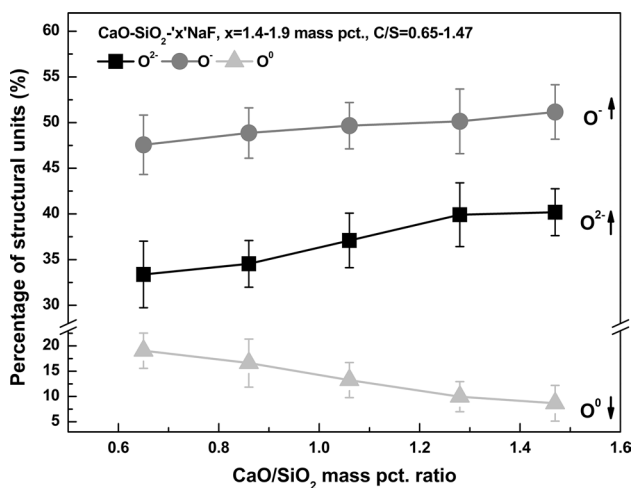


Fig. 10 Percentage of structural units of the deconvoluted XPS spectra at comparable NaF contents and C/S between 0.65 and 1.47

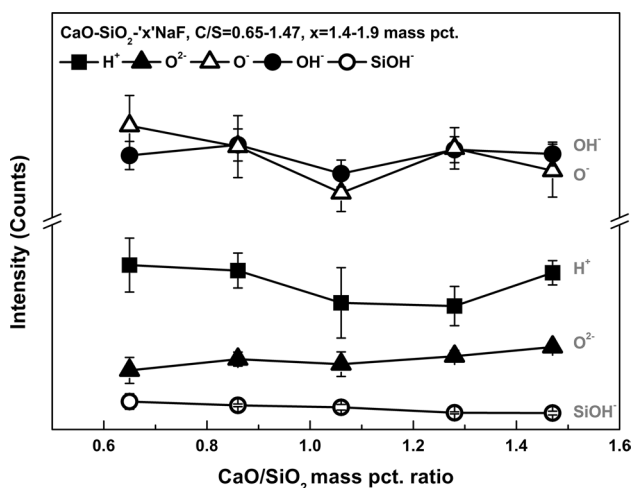


Fig. 11 TOF-SIMS spectra as a function of C/S at comparable NaF contents between 1.4 and 1.9 mass pct

and favoring the free hydroxyl mechanism for hydrogen dissolution.

Figure 10 shows the percentage of oxygen anion species after deconvolution of the XPS spectra as a function of C/S at NaF contents between 1.4 and 1.9 mass pct. With an increase in the C/S, the amount of available O²⁻ increased, which could consume O⁰ to produce O⁻, resulting in depolymerization of the silicate network structure. Again, excess O²⁻ at higher C/S diminished the amount of O⁰ available for hydroxyl incorporation and caused the free hydroxyl reaction to be the dominant hydrogen dissolution mechanism, which seems to be in good agreement with the FTIR and Raman results.

The XPS results also correlated closely with the TOF-SIMS results, as shown in Fig. 11. The parabolic behavior

of H⁺ as a function of C/S was similar to the hydrogen dissolution behavior analyzed by the RH-600. During the depolymerization reaction, O²⁻ reacts with O⁰ to generate O⁻. The increase in the amounts of O⁻ and O²⁻ at higher C/S is similar to the XPS results. Furthermore, the amount of incorporated hydroxyl (Si-OH⁻) decreased with an increase in the C/S and the amount of free hydroxyl (OH⁻) increased with the content of network-modifying components in the flux system, including CaO and NaF. The results of the structural analysis based on FTIR spectroscopy, Raman spectroscopy, XPS, and TOF-SIMS were found to correlate well with the hydrogen dissolution behavior observed for the present CaO-SiO₂-NaF flux system.

4 Conclusion

The effect of NaF and C/S on the hydrogen solubility in terms of the hydroxyl capacity and structure of a CaO-SiO₂-NaF flux system at 1823 K was studied. The addition of NaF affected the hydrogen solubility and flux structure of the system, which could modify the system's complex structure. In an acidic flux system dominated by incorporated hydroxyl, NaF reduced the available incorporated hydroxyl sites and subsequently lowered the hydroxyl capacity. For a basic flux system, NaF assisted in fully depolymerizing the flux system to increase the amount of free hydroxyl and hydroxyl capacity. Furthermore, a high C/S promoted the depolymerization of the network structure and simplified the structure. The mechanism of hydrogen solubility was dependent on the composition of the flux, where incorporated hydroxyl was dominant at low C/S and the free hydroxyl mechanism was dominant at high C/S. In the transition region, both incorporated and free hydroxyl co-existed in the flux system, and the effect of compositional changes on hydrogen dissolution and structural units in the flux correlated well. It is expected that the addition of NaF and C/S greater than 1.2 can be used in a welding flux system to capture hydrogen from the weld joint.

Acknowledgements This work was partially supported by the BK21PLUS Project in the Division of Eco-Humantronics Information Materials and supported by the Technology Innovation Program (No. 10052751) funded by the Ministry of Trade, Industry and Energy (MOTIE, Korea).

References

1. J.-E. Jin, Y.-K. Lee, *Advanced Steels* (Springer, Berlin, 2011), pp. 259–264
2. J.-E. Jin, Y.-K. Lee, *Acta Mater.* **60**, 1680–1688 (2012)
3. M. Koyama, E. Akiyama, Y.-K. Lee, D. Raabe, K. Tsuzaki, *Int. J. Hydrogen Energy* **6**, 2706–2723 (2017)

4. X. Zhu, K. Zhang, W. Li, X. Jin, *Mater. Sci. Eng. A* **658**, 400–408 (2016)
5. J. Venezuela, Q. Liu, M. Zhang, Q. Zhou, A. Atrens, *Corros. Sci.* **99**, 98–117 (2015)
6. J. Sojka, M. Sozańska, P. Váňová, V. Vodárek, F. Filuš, *Solid State Phenom.* **227**, 259–262 (2015)
7. Y.J. Yan, Y. Yan, Y. He, J.X. Li, Y.J. Su, L. Qiao, *Int. J. Hydrogen Energy* **39**, 17921–17928 (2014)
8. S.H. Chung, I. Sohn, *Metall. Mater. Trans. B* **50**, 991–999 (2019)
9. K.H. So, J.S. Kim, Y.S. Chun, *ISIJ Int.* **49**, 1952–1959 (2009)
10. J.-Y. Park, J.G. Park, C.H. Lee, I. Sohn, *ISIJ Int.* **51**, 889–894 (2011)
11. C.S. Chai, T.W. Eagar, *Weld. J.* **07**, 229–232 (1982)
12. P. Nevasmaa, *Weld. World* **48**, 2–18 (2004)
13. A.A. Omar, *Welding Research Supplement* (1998), pp. 86–93
14. L.E. Russell, *J. Soc. Glass Technol.* **41**, 304–317 (1957)
15. S.C. Shim, J.W. Choi, S.T. Hwang, K.C. Kim, *Korean J. Met. Mater.* **46**, 662–671 (2008)
16. J.H. Kiefer, *Weld. J.* **5**, 155–161 (1996)
17. S. Kimura, M. Furuya, A. Tanaka, *Tetsu-to-Hagane* **64**, 240–249 (1978)
18. T. Fukushima, Y. Iguchi, S. Banya, T. Fuwa, *Trans. ISIJ* **6**, 19–26 (1966)
19. J.L. Davidson, *Aust. Weld. J.* **43**, 33–39 (1998)
20. C. Wildash, R.C. Cochrane, R. Gee, D.J. Widgery, in *Proceedings of the 5th International Conference on Trends in Welding Research, 1–5 June, 1998 (Pine Mountain, USA)* (ASM International, 1999), pp. 745–750
21. M. Imai, H. Ooi, T. Emi, *Tetsu-to-Hagane* **48**, 111–117 (1962)
22. P.L. Sachdev, A. Majdic, H. Schenck, *Metall. Trans. B* **3**, 1537–1543 (1972)
23. J. Brandberg, D. Sichen, *Metall. Trans. B* **37B**, 389–393 (2006)
24. K. Schwerdtfeger, H.G. Shubert, *Metall. Trans. B* **9B**, 143–144 (1978)
25. J.W. Tomlinson, *J. Soc. Glass Technol.* **40**, 25–31 (1956)
26. J.H. Walsh, J. Chipman, T.B. King, N.J. Grant, *Trans. ISIJ* **206**, 1568–1576 (1956)
27. G.D. Chukin, V.I. Malevich, *J. Appl. Spectrosc.* **26**, 223–229 (1977)
28. B. Weckler, H.D. Lutz, *Eur. J. Solid State Org. Chem.* **35**, 531–544 (1998)
29. A.N. Murashkevich, A.S. Lavitskaya, T.I. Barannikova, I.M. Zhar-skii, *J. Appl. Spectrosc.* **75**, 730–734 (2008)
30. B.O. Mysen, D. Virgo, W.J. Harrison, C.M. Scarfe, *Am. Mineral.* **65**, 900–914 (1980)
31. J.-Y. Park, J.S. Han, I. Sohn, *ISIJ Int.* **51**, 1788–1794 (2011)
32. J.-Y. Park, S.J. Park, W.S. Chang, I. Sohn, *J. Am. Ceram. Soc.* **95**, 1756–1763 (2012)
33. J.-Y. Park, W.-S. Chang, I. Sohn, *Sci. Technol. Weld. Join.* **17**, 134–140 (2012)
34. S.H. Chung, J.-Y. Park, S.-J. Park, W.-S. Chang, I. Sohn, *ISIJ Int.* **53**, 27–33 (2013)
35. I.M. Kempson, T.J. Barnes, C.A. Prestidge, *J. Am. Soc. Mass Spectrom.* **21**, 254–260 (2010)
36. S.H. Chung, I. Sohn, *Int. J. Hydrogen Energy* **39**, 18490–18497 (2014)
37. S.-K. Jo, S.-H. Kim, *Steel Res. Int.* **71**, 15–21 (2000)
38. B.O. Mysen, D. Virgo, F.A. Seifert, *Rev. Geophys. Space Phys.* **20**, 353–383 (1982)
39. G.H. Kim, I. Sohn, *Metall. Mater. Trans. B* **42**, 1218–1223 (2011)
40. S. Ueda, H. Koyo, T. Ikeda, Y. Kariya, M. Maeda, *ISIJ Int.* **40**, 739–743 (2000)
41. J.H. Park, D.J. Min, *J. Non Cryst. Solids* **337**, 150–156 (2004)
42. G. Toop, C. Samis, *Trans. Metall. Soc. AIME* **224**, 870 (1962)

Publisher's Note Springer Nature remains neutral with regard to jurisdictional claims in published maps and institutional affiliations.